Dirac hierarchy in confined Mie resonance photonic crystals

Yuexin Zhang, Xiaoyu Dai, and Yuanjiang Xiang [*]

School of Physics and Electronics, Hunan University, Changsha 410082, China

The Dirac hierarchy (DH), comprising an eightfold bulk Dirac cone (DC), a fourfold surface DC, a twofold hinge, and a corner state, has been proposed and observed in acoustic systems recently. DH establishes a versatile platform for exploring exotic phenomena related to the hierarchy of Dirac physics and topological phases at varying dimensions. However, the investigation of DH in the context of photonic crystals is still lacking, as the electromagnetic interactions in the 3D configuration are complex and difficult to match with the tight-binding model. In this study, we first propose a photonic DH in the Mie-confined resonance framework with band chirality. DH with 2D surface states, 1D hinge states, and 0D corner states is obtained by lattice distortions. Besides, we extend the 3D framework to the disclination-introduced photonic system and prove the coexistence of robust disclination, corner, and hinge states. Our work explores the Dirac physics in photonics, offers insights to manipulate electromagnetic waves at varying dimensions, and reveals unconventional bulk-disclination correspondence in 3D photonic materials.

I. INTRODUCTION

Over the past decades, the success of topological insulators (TIs) has injected vitality into condensed matter physics [1–4]. These TIs, protected by band topology theory [5], have enabled unconventional bulk-boundary correspondence, allowing the control of unidirectional waves across platforms such as acoustics, photonics, and circuits [6–11]. In addition, there have been exciting discoveries and artificial fabrications of novel topological materials based on spatial symmetry and time-reversal-symmetry reflection [12–14]. Among these findings, the Dirac cone (DC) observed in 2D graphene lattices has attracted attention due to its massless properties in electronic systems [15–18]. Currently, the discovery of higher-order topological insulators (HOTIs) has provided deeper insights into lower-dimensional topological systems [19–27]. In 3D HOTI, DCs are classified into bulk, surface, and hinge versions, forming what is known as the Dirac hierarchy (DH). This concept has been implemented in acoustic crystals by introducing a multilayer sonic monolayer lattice to achieve in-plane and out-of-plane distortions [28–30].

Until now, DH in 3D photonic crystals (PhCs) has been limited due to complex electromagnetic (EM) properties compared to sonic waves. Moreover, the decay rate of the Mie resonances' states in dielectric photonic HOTIs is slow, resulting in distinct physics between the tight-binding model (TBM) and dielectric PhCs, and hence the band chiral symmetry is no longer protected [31]. In addition, the DH structure typically preserves C_n symmetry, forming what is known as topological crystalline insulators (TCIs), which have been extensively studied in 2D systems to reveal bulk-disclination correspondence with boundary-localized fractional charge

[32–34]. However, the disclination defect is rarely discussed in 3D PhCs. Therefore, it is promising that we can bring DH into 3D photonic platforms and even defect-introduced systems to capture multiple topological phases, which ushers in new approaches to exploring the coexistence of HOTI phases and defect modes in 3D frameworks.

Here, we propose a refined dielectric PhC with confined Mie resonance. The unit cell consists of a stacked 2D TCI connected with a 1D vertical Su-Schrieffer-Heeger (SSH) chain. The central and lateral regions of the structure are inserted with metal pillars to allow exponential decay of Mie resonance states, and drilled metal plates provide vertical couplings. This design guarantees the chiral symmetric band dispersions that resemble those observed in a TBM. By changing the horizontal and vertical directional couplings, the DC will split into lower dimensions in an orderly manner. 0D corner modes can be obtained by constructing C_n-symmetric TCIs or breaking mirror symmetry. More importantly, the idea of confined Mie resonance PhCs can be used to study 3D disclination-introduced PhCs. By establishing the multilayer finite-size plate through the "cut-and-glue" method, we observe robust 1D hinge, 0D corner, and disclination modes simultaneously. Our research has not only broadened Dirac physics in photonic HOTIs, but has also extended topological phases with bulk-disclination correspondence from 2D to 3D versions.

II. MODEL CONSTRUCTIONS

We introduce the PhC model based on the TBM as depicted in Fig. 1(a). The unit cell consists of two components: the double-layer honeycomb lattices and the vertical SSH chains. The eightfold bulk DC is maintained when the ratios of in-plane inter- and intracell couplings (t_1 and t_0) and out-of-plane inter- and intralayer hopping (t_{z1} and t_{z0}) are both equal to 1

---

[*]xiangyuanjiang@126.com
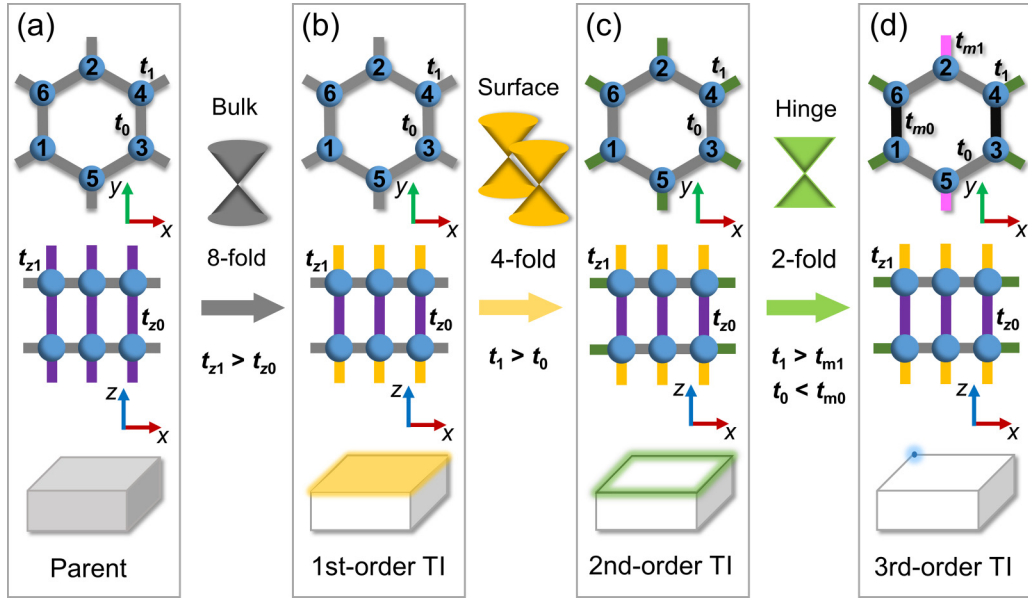
FIG. 1. The TBM of our PhC and corresponding topological phase transition process. (a) The eightfold DC ($t_{z1}/t_{z0} = t_1/t_0 = 1$). (b) The fourfold surface DC ($t_{z1}/t_{z0} > 1$). (c) The twofold hinge DC between the surface band gap ($t_1/t_0 > 1$). (d) The third-order corner mode ($t_1 > t_{m1}$, $t_0 < t_{m0}$).

[Fig. 1(a)]. When $t_{z1}/t_{z0} > 1$, the SSH chain exhibits topological behavior, causing the bulk DC to split into a fourfold surface DC [Fig. 1(b)]. Subsequently, by setting $t_1/t_0 > 1$, the surface DC becomes gapped, the structure manifests a HOTI phase, and a twofold hinge DC appears [Fig. 1(c)]. Furthermore, a third-order corner mode occurs by breaking the mirror symmetry ($t_1/t_{m_1} > 1$, $t_0/t_{m_0} < 1$) [Fig. 1(d)]. Thus, we derive the complete hierarchy picture in a 3D framework with different topological phases at specific dimensions. Our model can be expressed as the Hamiltonian matrix [28],

$$H(\mathbf{q}) = H_z \otimes I_6 + I_2 \otimes H_{xy}, \quad (1)$$

where $H_z = (t_{z0} + t_{z1} \cos q_z)\sigma_x + \sin q_z \sigma_y$ represents the SSH Hamiltonian, σ_x and σ_y are Pauli matrices, and I_2 and I_6 are 2×2 and 6×6 identity matrices, respectively. $H_{xy} = [0, \mathbf{h}(q_x, q_y); \mathbf{h}^*(q_x, q_y), 0]$ is the monolayer hexagonal lattice Hamiltonian with $\mathbf{h}(q_x, q_y) = [t_1 e^{(iq_x + iq_y)}, t_0, t_0; t_0, t_1 e^{-2iq_y}, t_0; t_0, t_0, t_1 e^{(-iq_x + iq_y)}]$, and $\mathbf{q}(q_x, q_y, q_z)$ is the normalized wave vector in momentum space, where $q_x = k_x/2$, $q_y = \sqrt{3}k_y/2$, and $q_z = k_z$. Apparently, H_z satisfies the chiral symmetry $\Gamma_z H_z \Gamma_z = -H_z$, where $\Gamma_z^2 = 1$. In this way, the eigenenergy of the system is written as $E = E_{xy} + E_z$, denoting the in-plane honeycomb lattice eigenenergy E_{xy} and the vertical SSH chain eigenenergy E_z [28]. Similarly, the complete set of eigenstates of the model is delivered into two parts: $\Psi = \Psi_{xy} \otimes \Psi_z$, where Ψ_{xy} (Ψ_z) is the eigenstate of E_{xy} (E_z). It is noticed that the hierarchy can be interpreted via the classifications of Ψ_{xy} (Ψ_z). We have the following: if Ψ_{xy} and Ψ_z are bulk states, the system keeps bulk modes. If Ψ_z keeps topological and Ψ_{xy} remains the bulk state, the parent structure supports surface states. If Ψ_{xy} is the edge state (or in-plane corner state) and Ψ_z is the edge mode, the system will feature the 1D hinge (or 3D corner) state.

Figure 2(a) illustrates a 3D view of the proposed lattice TBM. The unit cell consists of two single-layer honeycomb lattices connected by SSH chains. The real design of the PhC consists of bifurcated dielectric rods with metal pillars embedded between the dielectric rods [Fig. 2(b)]. Each dielectric pillar has three branches that interact with the nearest dielectric pillar. In the classical wave environment, the lattice allows propagation solutions at every frequency. That is, the lower bands are plane-wave-like, while the higher bands are TBM-like [35], and the chiral symmetry of the energy bands around the zero-energy line is no longer protected. In this regard, metal rods can be inserted between dielectric pillars,
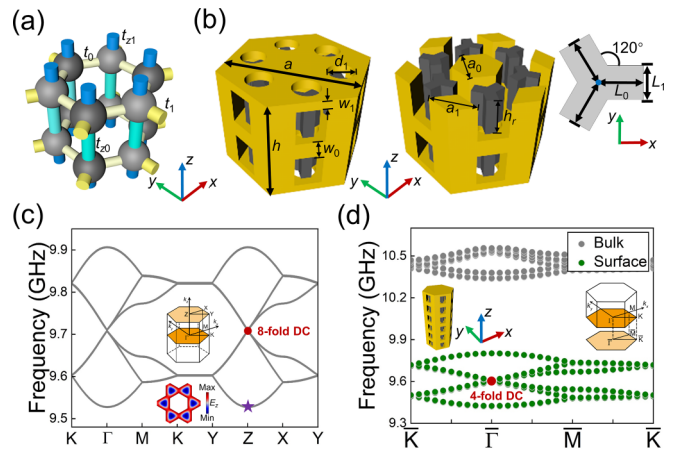
FIG. 2. Design and the band spectrum of our 3D PhC. (a) TBM of the PhC. (b) Architecture of the unit cell. (c) The bulk band structure of the model at $t_{z1}/t_{z0} = t_1/t_0 = 1$. The 3D Brillouin zone (BZ) and the lowest eigenmode profile. (d) Band dispersions of the surface modes. The inset view presents the piling supercell and the projected 2D BZ.

which confine the slowly decaying Mie resonances' states [36]. The E_z components of the lattice shown in Fig. 2(c) shows a localized field around the scatters at the lowest band (purple star). For PhCs without embedded metal rods, the eigenmode profile of the lowest band shows linear dispersion and plane wave behavior; see the Supplemental Material [37]. Metallic rods between dielectric pillars form the structure that strengthens the nearest-neighbor hopping of the two isolated scatters. EM wave propagation in such lattice configurations can be well matched with the TBM.

III. DIMENSIONAL HIERARCHY

The directional couplings are realized as follows. By altering the radius of the inserted metallic rods, we can control the in-plane coupling terms, while the out-of-plane coupling can vary by tuning the sizes of drilled holes, as described in Fig. 2(b). The initial parameters are given as follows: the lattice constant $a = 30\,\text{mm}$ and $h = 24\,\text{mm}$, the width (length) of each bifurcated bar $L_1 = 2.4\,\text{mm}$ ($L_0 = 3.6\,\text{mm}$), the size of the central (side) metallic pillar $a_0 = 0.4a$ ($a_1 = 0.4a$), the thickness of the top (bottom) metal plate $w_1 = 2\,\text{mm}$ ($w_0 = 2w_1$), the height of the dielectric rod $h_r = 8\,\text{mm}$, the radius of the top and bottom (middle) drilled holes $d_1 = d_0 = 2.4\,\text{mm}$, and the relative dielectric permittivity of dielectric rods $\varepsilon = 9$. The distance between two nearest dielectric rods is fixed as $l = a/3$. For the original eightfold bulk DC ($t_{z1}/t_{z0} = 1$), the degeneracy occurs at the Z point (red solid dot), as shown in Fig. 2(c). Throughout this paper, all full-wave simulations and numerical calculations are performed using the finite element method software COMSOL Multiphysics.

A. First-order hierarchy with surface Dirac cone

To establish a topological SSH chain within our PhC model ($t_{z1}/t_{z0} > 1$), we adjust the sizes of holes d_0 and d_1 to be 2.4 mm and 6.4 mm, respectively, where a larger hole corresponds to a stronger hopping strength. The eightfold DC will collapse, and the first-order DH is obtained. We construct a multilayer supercell consisting of three PhCs, with top and bottom plates undrilled to create perfect electric conductor (PEC) boundaries in the z direction, as shown in the inset of Fig. 2(d). The surface band dispersions of nontrivial SSH chains along $\bar{K}$-$\bar{\Gamma}$-$\bar{M}$-$\bar{K}$ are shown in Fig. 2(d), where the surface states span the range of 9.4–9.8 GHz. The fourfold DC appears at about 9.6 GHz at the $\bar{\Gamma}$ point (red solid dot). To further investigate surface wave transmission, we construct a three-layer finite-size architecture to perform a full-wave simulation; see the Supplemental Material [37].

The introduction of the nontrivial SSH chain ($t_{z1} > t_{z0}$) splits the band, and the eightfold Dirac cone is lifted into two Dirac cones at the A point ($k_z = \pi$), as shown in the upper panel of Fig. 3(b). To distinguish between the two phases, we need to further examine the band properties of the degeneracy bands at the A point from band 3 to band 10 (counting from the bottom band). For the eightfold degeneracy, the eigenstate profiles have a pair of chiral partners with symmetric (S) and asymmetric (A) modes. We have highlighted the bands with A modes in orange color and S modes in gray color. Figure 3(a) illustrates the mode profiles at the A point with the SSH chain
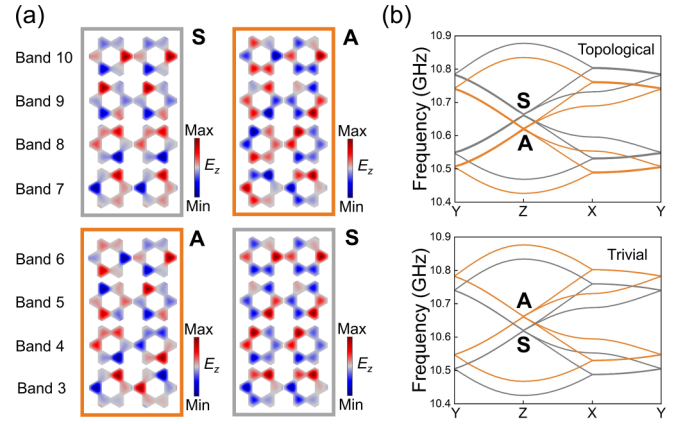
FIG. 3. Bands and eigenfields of the trivial and topological SSH chain in the confined Mie resonance PhC. (a) Left part: Simulations of the topological SSH chain's eight eigenmode profiles at the Z point. Right part: The eigenmode profiles at the Z point for trivial SSH chain. (b) The band structures of the topological and trivial unit cell along the path Y-Z-X-Y.

of $t_{z1} > t_{z0}$ and $t_{z1} < t_{z0}$, respectively. The eigenmode profiles at the top and bottom parts of the unit cell show that the bands 3–6 are A modes (S modes) and bands 7–10 are S modes (A modes) for the nontrivial (trivial) SSH chain. Both cases exhibit dipole p and quadrupole d natures. This indicates a phase transition process along the vertical direction, which is independent of the in-plane couplings.

B. Second-order hierarchy with hinge Dirac cone

To achieve the second-order hierarchy, we further adjust the in-plane couplings of the honeycomb lattice. By setting $a_0 = 0.4a$ and $a_1 = 0.34a$ while keeping other parameters unchanged, the 2D hexagonal lattice is topological and exhibits second-order edge states. Figure 4(a) provides in-plane views of two types of hinges, the armchair-typed hinge (A hinge) and the zigzag-typed hinge (Z hinge), with periodic boundary conditions in the x direction and PEC boundaries in the y direction. The hinge band dispersions of the A hinge and Z hinge are calculated and presented in Figs. 4(d) and 4(e), respectively. For the A hinge, the second-order hinge modes traverse the surface band gap in the frequency range of approximately 8.65–8.95 GHz with a band gap, while for the Z hinge the twofold DC emerges at about 8.8 GHz. To investigate the transmission of hinge modes, we construct a second-order piled PhC sample, as shown in Fig. 4(b). In this configuration, the source (red solid circle) is positioned on the left edge of the sample, the hinge probe (blue solid circle) is located on the right edge, and the surface probe (green solid circle) is inserted into the top plate of the structure. The upper panel of Fig. 4(c) computes the hinge wave transmission on the top layer at the excitation frequency of 8.87 GHz, while the lower panel shows the surface state on the top layer at 8.94 GHz. Additionally, Fig. 4(f) presents the $|E_z|$ intensity profile of surface states (green region) and hinge states (blue region) spanning 8.6–9.0 GHz, which closely aligns with the hinge dispersion shown in Fig. 4(d). It is noticed that the A hinge hosts a hinge band gap (light blue region), where corner
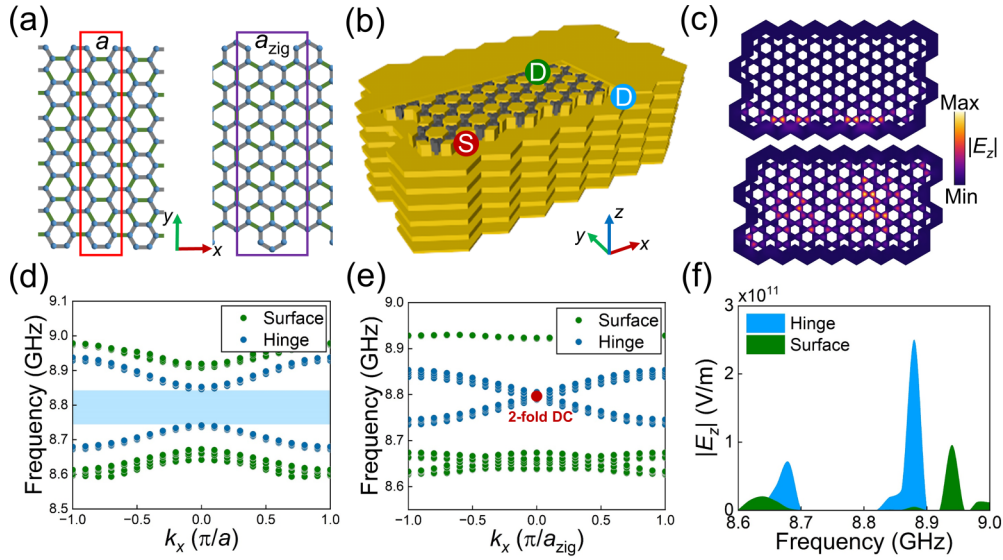
FIG. 4. Constructions of the *A* hinge and *Z* hinge. (a) The schematic graph of the periodic supercell array in the *x* direction for *A* hinge and *Z* hinge, respectively. (b) 3D view of the piling finite-size sample. (c) Upper panel: $|E_z|$ field distribution of hinge modes at 8.88 GHz. Lower panel: $|E_z|$ field distribution of surface modes at 8.94 GHz. (d) and (e) Hinge band diagrams for *A* hinge and *Z* hinge, respectively. The twofold 1D *Z* hinge DC appears in the surface band gap. (f) Simulated $|E_z|$ field intensity profiles of hinge and surface state ranging from 8.6–9.0 GHz.

modes will generate in the band gap. This can be illustrated by the topological invariant index for the existence of HOTI phases in a TCI [38,39]; see Supplemental Material [37].

C. Third-order hierarchy with corner states

Finally, to achieve the third-order hierarchy with the 0D corner mode, we introduce two approaches: constructing a C_n-symmetric TCI in the *xy* plane while maintaining a nontrivial SSH chain, or breaking the mirror symmetry of the unit cell, as depicted in Figs. 5(a) and 5(c), respectively. In the first approach, we maintain the same model parameters as in the second-order hierarchy. The higher-order topological properties of PhC are measured with the topological invariant index [38,39], which is thoroughly analyzed in the Supplemental Material [37]. The 0D corner state will emerge in the piled armchair-rhombus-shaped (ARS) sample. Consequently, the corner mode occurs at the top corner of the architecture. Figure 5(b) illustrates the eigenmode of the corner state at a frequency of 8.79 GHz. In Fig. 5(e), we present the solution numbers of the ARS structure, where four corner modes (orange solid dots) are located within the band gap region, situated between hinge states (blue solid dots) and surface states (green solid dots). To detect the corner state, we position a source (red solid circle) near the top corner of the sample, while the corner (orange solid circle), hinge (blue solid circle), and surface (green solid circle) probes are placed in corresponding locations, as shown in Fig. 5(a). The inset view of Fig. 5(e) displays the $|E_z|$ field distributions of corner (orange region), hinge (blue region), and surface (green region) waves, which are in excellent agreement with the eigenmode solution diagram. Figure 5(b) demonstrates the corner mode with the source excitation frequency at 8.79 GHz on the top surface.

In the second approach, we exploit the broken mirror symmetry to obtain the corner state in a zigzag-rhombus-shaped

(ZRS) sample, as depicted in Fig. 5(c). The distortion of intra- and intercell couplings (with $t_1 > t_{m1}$ and $t_0 < t_{m0}$) in a real PhC can be achieved by adjusting the L_0 between dielectric rods. Based on Fig. 1(d), we set the L_0 of two bifurcated branches to be $0.13a$ and $0.11a$ to ensure $t_0 < t_{m0}$ and $t_1 > t_{m1}$; see Supplemental Material [37]. This configuration results in broken mirror symmetry in the *x* direction, causing the corner modes at 8.75 GHz, as depicted in Fig. 5(d). In Fig. 5(c), we position the source and probes to simulate the corner, hinge, and surface states, similar to the approach used in the previous ARS model. Figure 5(f) presents the top slice of the $|E_z|$ field distribution corresponding to the corner state at 8.75 GHz. The inset views in Fig. 5(f) display the computed $|E_z|$ intensity profiles of corner (orange region), hinge (blue region), and surface (green region) states in a ZRS sample. These profiles are consistent with the frequency distributions of the solution numbers.

IV. DISCLINATION-INTRODUCED TOPOLOGICAL HIERARCHY

Inspired by the multilayer finite-size PhCs, it is natural to associate the DH model with the disclination defects in 2D TCIs, which is produced by inserting or deleting $1/n$ part (Frank angle $\Omega = 2\pi/6$) of the C_n-symmetric plate [32–34,39,40]. With the cut-and-glue process, the disclination defect will appear in the central region, as shown in Fig. 6(b). We extend the 2D disclination model to the 3D hierarchy framework. Figure 6(a) illustrates the building of the topological PhC with a metal rod embedded in the center of the lattice. The in-plane layout of the hexagonal lattice is similar to the unit cell shown in Fig. 2(b), except for the placement of dielectric rods and the removal of side metal rods. The deformed PhC's TBM is provided in the Supplemental Material [37]. The lattice parameters are listed below. The lattice
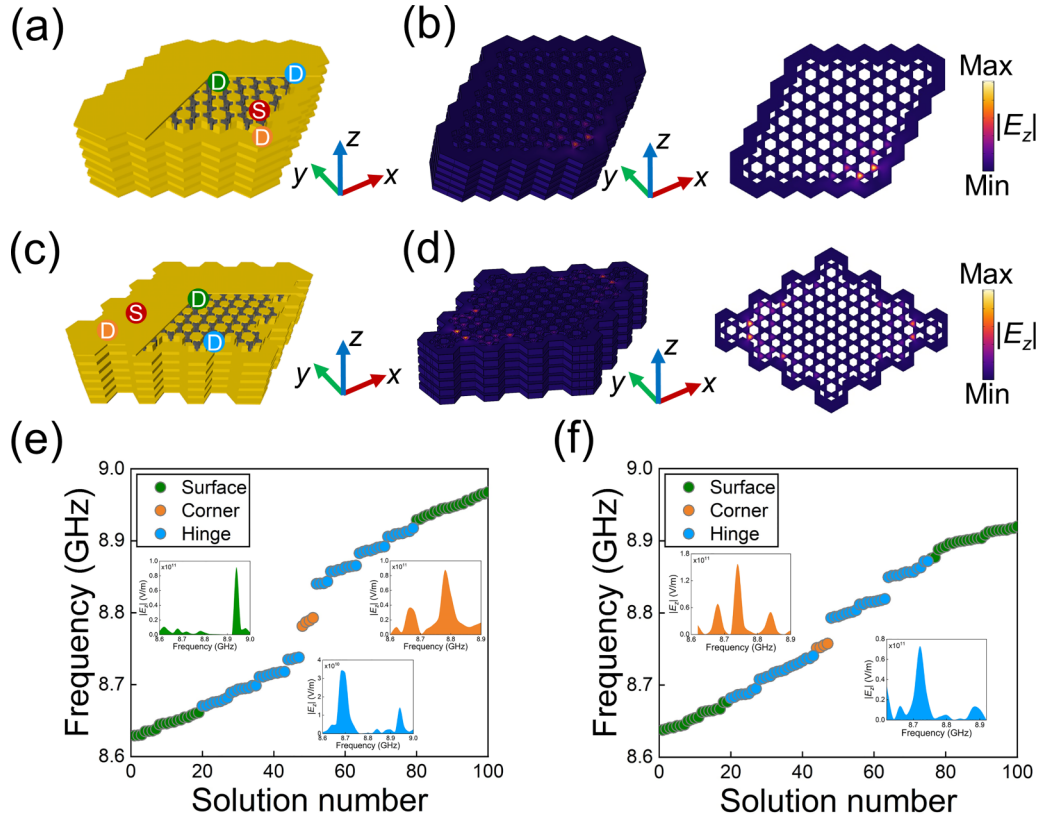
FIG. 5. Illustrations of the third-order hierarchy in ARS and ZRS configurations. (a) The finite-size multilayer ARS structure. (b) 3D view and the top slice of the $|E_z|$ field profile with exaction frequency of 8.78Hz in the ARS sample. (c) The multilayer ZRS sample. (d) 3D view and the top slice of the $|E_z|$ field profile with exaction frequency of 8.75 GHz in the ZRS model. (e) and (f) Solution numbers of the corner, hinge, and surface states and corresponding $|E_z|$ spectrum for ARS and ZRS schemes, respectively.
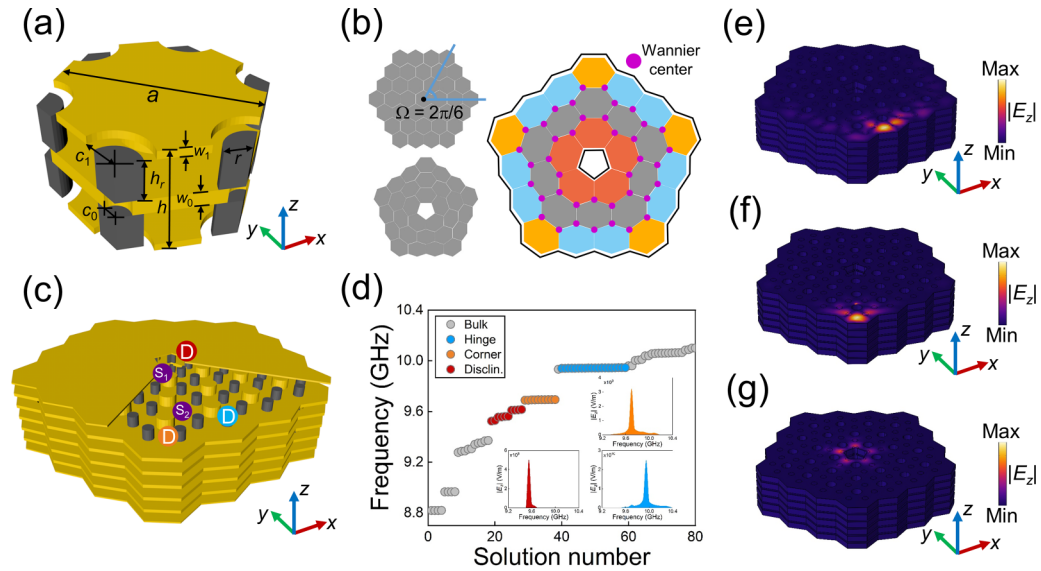
FIG. 6. Description of the PhC for generating disclination modes in a 3D structure. (a) The 3D view of the expanded unit cell. (b) Left panel: The cutting-and-glue operation for producing defect plate. Right panel: The Wannier center distributions for a topological meta-plane. (c) Construction of the multilayer finite-size disclination structure. (d) Solution numbers of the hinge, corner, and disclination states and corresponding $|E_z|$ profiles, respectively. (e)–(g) $|E_z|$ distributions of hinge, corner, and disclination modes at 9.95, 9.70, and 9.55 GHz, respectively.
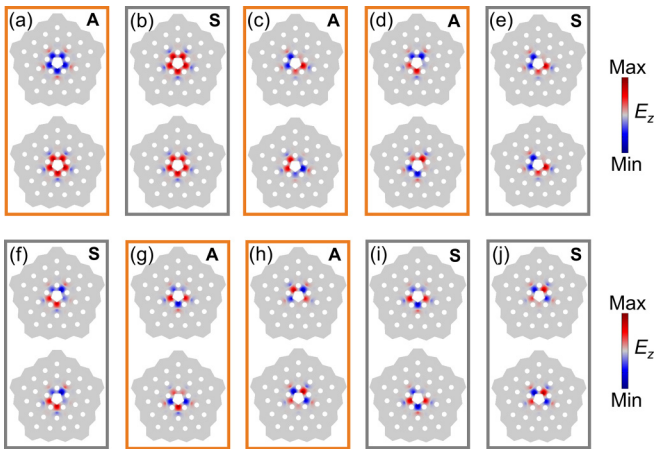
FIG. 7. Simulations on real space stacking hexagonal-shaped PhC arrays with eigenmode profiles for disclination modes.

constant $a = 24$ mm ($h = 14$ mm), the radius of dielectric rods (central metal rod) $r = 5$ mm ($R = 5$ mm), $w_1 = 1$ mm, $w_0 = 2w_1$, the radius of top (central) drilled holes $c_1 = 1.4r$ ($c_0 = 0.6r$), the distance between adjacent dielectric rods $l = a/\sqrt{3}$. The right part of Fig. 6(b) marks the Wannier centers (purple dots) in a nontrivial case, where the corner charge appears due to the principle of fractional charge distribution in the HOTI phase [32,33,39,40]. In Fig. 6(c), we construct a three-layer disclination-introduced architecture consisting of deformed PhCs in both in-plane and out-of-plane directions. We calculate the eigenmode solutions of the sample and find a dimensional hierarchy from hinge (blue dots) to corner (orange dots) to disclination (red dots) modes, as pictured in Fig. 6(d). To examine the coexistence of HOTI phases and disclination modes, we analytically excite these modes by placing two sources near the top center (S_1) and near the top corner (S_2), and three detectors are put to receive hinge (blue solid circle), corner (orange solid circle), and disclination (red solid circle), respectively. The inset of Fig. 6(d) gives the corresponding mode intensity profile $|E_z|$, matching well with the solution numbers. Figures 6(e)–6(g) show the $|E_z|$ distribution of hinge, corner, and disclination states at 9.95, 9.70, and 9.55 GHz, indicating robust EM wave transmission and concentration in the presence of topological defects.

It is known that a 2D C_n-symmetric unit cell has n sectors. Protected by the C_n symmetry, the lattice keeps invariant under the n-fold rotational operation. The disclination mode will emerge in the trapped central defect if we deform the finite-size C_n-symmetric plate. Following this, the 3D multilayer sample will support disclination modes if we adopt the honeycomb-SSH-like piling method to generate DH, where the 0D disclination mode will appear on the top and the bottom surface of the sample. Figure 7 gives ten eigenmode profiles of disclination state of the sample in Fig. 6(c), where the top (bottom) profile in each box represent the eigenmode at the top (bottom) surface of the configuration. It is evident that there are five A modes (orange box) and five S modes (gray box), respectively.

V. CONCLUSIONS

In this work, we propose a photonic DH in a refined Mie-confined honeycomb-SSH PhC. By carefully adjusting the in-plane and out-of-plane coupling strengths, we obtain a series of topological phases at different dimensions based on the parent configurations. The introduction of metal pillars and drilled metal plates in the model ensures the chirality of the band spectrum and vertical modulation. We offer two approaches to achieving the third-order hierarchy. Analysis indicates a complete bulk-surface-hinge-corner correspondence in distinct samples with zigzag and armchair hinges. EM wave excitation on finite-size multilayer architectures shows robust surface and hinge wave propagation, as well as strongly localized corner modes. In addition, we develop the DH and introduce a model that supports the coexistence of corner, hinge, and disclination phases with topological defects. These findings open up possibilities for the fabrication of high-performance optical devices with EM wave storage and transmission at different dimensions, paving the way for exciting advances in photonics.

[1] K. v. Klitzing, G. Dorda, and M. Pepper, New method for high-accuracy determination of the fine-structure constant based on quantized Hall resistance, Phys. Rev. Lett. **45**, 494 (1980).

[2] L. Fu, C. L. Kane, and E. J. Mele, Topological insulators in three dimensions, Phys. Rev. Lett. **98**, 106803 (2007).

[3] M. Z. Hasan and C. L. Kane, *Colloquium*: Topological insulators, Rev. Mod. Phys. **82**, 3045 (2010).

[4] X. Zhang, F. Zangeneh-Nejad, Z.-G. Chen, M.-H. Lu, and J. Christensen, A second wave of topological phenomena in photonics and acoustics, Nature (London) **618**, 687 (2023).

[5] A. Bansil, H. Lin, and T. Das, *Colloquium*: Topological band theory, Rev. Mod. Phys. **88**, 021004 (2016).

[6] A. B. Khanikaev, S. H. Mousavi, W.-K. Tse, M. Kargarian, A. H. MacDonald, and G. Shvets, Photonic topological insulators, Nat. Mater. **12**, 233 (2013).

[7] W. Song, W. Sun, C. Chen, Q. Song, S. Xiao, S. Zhu, and T. Li, Robust and broadband optical coupling by topological waveguide arrays, Laser Photon. Rev. **14**, 1900193 (2020).

[8] X. Ni, M. Weiner, A. Alu, and A. B. Khanikaev, Observation of higher-order topological acoustic states protected by generalized chiral symmetry, Nat. Mater. **18**, 113 (2019).

[9] G. Ma, M. Xiao, and C. T. Chan, Topological phases in acoustic and mechanical systems, Nat. Rev. Phys. **1**, 281 (2019).

[10] G.-G. Liu, Z. Gao, Q. Wang, X. Xi, Y.-H. Hu, M. Wang, C. Liu, X. Lin, L. Deng, S. A. Yang, P. Zhou, Y. Yang, Y. Chong, and B. Zhang, Topological Chern vectors in three-dimensional photonic crystals, Nature (London) **609**, 925 (2022).

[11] P. Zhu, X.-Q. Sun, T. L. Hughes, and G. Bahl, Higher rank chirality and non-Hermitian skin effect in a topolectrical circuit, Nat. Commun. **14**, 720 (2023).

[12] J. Langbehn, Y. Peng, L. Trifunovic, F. von Oppen, and P. W. Brouwer, Reflection-symmetric second-order topological insulators and superconductors, Phys. Rev. Lett. **119**, 246401 (2017).

[13] M. Ezawa, Topological switch between second-order topological insulators and topological crystalline insulators, Phys. Rev. Lett. **121**, 116801 (2018).

[14] T. Zhang, P. Cheng, X. Chen, J.-F. Jia, X. Ma, K. He, L. Wang, H. Zhang, X. Dai, Z. Fang, X. Xie, and Q.-K. Xue, Experimental demonstration of topological surface states protected by time-reversal symmetry, Phys. Rev. Lett. **103**, 266803 (2009).

[15] A. H. Castro Neto, F. Guinea, N. M. R. Peres, K. S. Novoselov, and A. K. Geim, The electronic properties of graphene, Rev. Mod. Phys. **81**, 109 (2009).

[16] D. Hsieh, Y. Xia, D. Qian, L. Wray, J. H. Dil, F. Meier, J. Osterwalder, L. Patthey, J. G. Checkelsky, N. P. Ong, A. V. Fedorov, H. Lin, A. Bansil, D. Grauer, Y. S. Hor, R. J. Cava, and M. Z. Hasan, A tunable topological insulator in the spin helical Dirac transport regime, Nature (London) **460**, 1101 (2009).

[17] X. Jiang, C. Shi, Z. Li, S. Wang, Y. Wang, S. Yang, S. G. Louie, and X. Zhang, Direct observation of Klein tunneling in phononic crystals, Science **370**, 1447 (2020).

[18] Q. Zhang, D. Lee, L. Zheng, X. Ma, S. I. Meyer, L. He, H. Ye, Z. Gong, B. Zhen, K. Lai, and A. T. C. Johnson, Gigahertz topological valley Hall effect in nanoelectromechanical phononic crystals, Nat. Electron. **5**, 157 (2022).

[19] W. A. Benalcazar, B. A. Bernevig, and T. L. Hughes, Quantized electric multipole insulators, Science **357**, 61 (2017).

[20] Q. Wei, X. Zhang, W. Deng, J. Lu, X. Huang, M. Yan, G. Chen, Z. Liu, and S. Jia, 3D hinge transport in acoustic higher-order topological insulators, Phys. Rev. Lett. **127**, 255501 (2021).

[21] Z. Song, Z. Fang, and C. Fang, $(d-2)$-dimensional edge states of rotation symmetry protected topological states, Phys. Rev. Lett. **119**, 246402 (2017).

[22] Y. Zhang, Z. Li, S. Xu, and Y. Xiang, Tunable and reconfigurable higher-order topological insulators in photonic crystals with phase change materials, Ann. Phys. **534**, 2100293 (2022).

[23] B.-Y. Xie, G.-X. Su, H.-F. Wang, H. Su, X.-P. Shen, P. Zhan, M.-H. Lu, Z.-L. Wang, and Y.-F. Chen, Visualization of higher-order topological insulating phases in two-dimensional dielectric photonic crystals, Phys. Rev. Lett. **122**, 233903 (2019).

[24] Y. Yang, J. Lu, M. Yan, X. Huang, W. Deng, and Z. Liu, Hybrid-order topological insulators in a phononic crystal, Phys. Rev. Lett. **126**, 156801 (2021).

[25] M. Li, D. Zhirihin, M. Gorlach, X. Ni, D. Filonov, A. Slobozhanyuk, A. Alù, and A. B. Khanikaev, Higher-order topological states in photonic kagome crystals with long-range interactions, Nat. Photon. **14**, 89 (2020).

[26] H. Qiu, M. Xiao, F. Zhang, and C. Qiu, Higher-order Dirac sonic crystals, Phys. Rev. Lett. **127**, 146601 (2021).

[27] Y. Qi, C. Qiu, M. Xiao, H. He, M. Ke, and Z. Liu, Acoustic realization of quadrupole topological insulators, Phys. Rev. Lett. **124**, 206601 (2020).

[28] L.-Y. Zheng and J. Christensen, Dirac hierarchy in acoustic topological insulators, Phys. Rev. Lett. **127**, 156401 (2021).

[29] L. Yang, Y. Wang, Y. Meng, Z. Zhu, X. Xi, B. Yan, S. Lin, J. Chen, B.-J. Shi, Y. Ge, S.-Q. Yuan, H. Chen, H.-X. Sun, G.-G. Liu, Y. Yang, and Z. Gao, Observation of Dirac hierarchy in three-dimensional acoustic topological insulators, Phys. Rev. Lett. **129**, 125502 (2022).

[30] Y. Zhang, J. Tang, X. Dai, and Y. Xiang, Flexible dimensional hierarchy of higher-order topology in the stacked kagome-chain acoustic crystal, Commun. Phys. **6**, 130 (2023).

[31] Z. Wang, D. Liu, H. T. Teo, Q. Wang, H. Xue, and B. Zhang, Higher-order Dirac semimetal in a photonic crystal, Phys. Rev. B **105**, L060101 (2022).

[32] Y. Liu, S. Leung, F.-F. Li, Z.-K. Lin, X. Tao, Y. Poo, and J.-H. Jiang, Bulk-disclination correspondence in topological crystalline insulators, Nature (London) **589**, 381 (2021).

[33] C. W. Peterson, T. Li, W. Jiang, T. L. Hughes, and G. Bahl, Trapped fractional charges at bulk defects in topological insulators, Nature (London) **589**, 376 (2021).

[34] Y. Deng, W. A. Benalcazar, Z.-G. Chen, M. Oudich, G. Ma, and Y. Jing, Observation of degenerate zero-energy topological states at disclinations in an acoustic lattice, Phys. Rev. Lett. **128**, 174301 (2022).

[35] E. Lidorikis, M. M. Sigalas, E. N. Economou, and C. M. Soukoulis, Tight-binding parametrization for photonic band gap materials, Phys. Rev. Lett. **81**, 1405 (1998).

[36] J. Li, H. Wang, S. Jia, P. Zhan, M. Lu, Z. Wang, Y. Chen, and B.-Y. Xie, Disentangled higher-orbital bands and chiral symmetric topology in confined Mie resonance photonic crystals, arXiv:2304.08179.

[37] See Supplemental Material at http://link.aps.org/supplemental/10.1103/PhysRevB.109.064105 for band properties of the PhC in absence of embedded metallic rods; the band properties of the first-order hierarchy; the analysis of the topological invariant index of designed PhC structure; the second-order hierarchy with 1D zigzag-shaped hinges and third-order hierarchy with mirror-broken operation; and the disclination mode in the 3D photonic piling architecture.

[38] X.-Y. Dong and C.-X. Liu, Classification of topological crystalline insulators based on representation theory, Phys. Rev. B **93**, 045429 (2016).

[39] W. A. Benalcazar, T. Li, and T. L. Hughes, Quantization of fractional corner charge in C_n-symmetric higher-order topological crystalline insulators, Phys. Rev. B **99**, 245151 (2019).

[40] T. Li, P. Zhu, W. A. Benalcazar, and T. L. Hughes, Fractional disclination charge in two-dimensional C_n-symmetric topological crystalline insulators, Phys. Rev. B **101**, 115115 (2020).